UDC 621.311:621.314.5 https://doi.org/10.20998/2074-272X.2026.3.06

Y. Daili, R. Bentafer, N. Djaraf, A. Harrag

Comprehensive modeling of grid-connected inverters in weak grid systems

Introduction. *The stability of grid-connected inverters is critical for the integration of renewable energy into modern power systems. However, this stability is significantly challenged under weak grid conditions, characterized by high impedance and low short-circuit ratios.* ***Problem.*** *Under such conditions, complex dynamic interactions arise between the inverter control systems, the grid, and the phase-locked loop, which is essential for synchronization. These interactions can degrade phase tracking and even lead to system instability. Such complexities render traditional models inadequate for accurately evaluating system behavior or guiding robust control design. The* ***goal*** *of this work is to develop and validate a compact, linearized state-space model of a grid-connected inverter under weak grid conditions, enabling stability analysis and supporting the design of robust control strategies.* ***Methodology.*** *Using small-signal modeling, a state-space representation of the inverter system is derived, incorporating control dynamics, grid impedance, and the power converter. The model's accuracy is validated through detailed nonlinear simulations, ensuring strong consistency between both modeling approaches.* ***Results.*** *The proposed model effectively captures the interaction between inverter dynamics and weak grid characteristics. Simulation results demonstrate a high correlation with nonlinear behavior, confirming the model's validity.* ***Scientific novelty.*** *Unlike existing models, this unified linearized state-space model explicitly captures cross-coupling effects among control loops and grid dynamics under weak grid scenarios. It enables more accurate stability analysis and provides deeper insights into the system's dynamic behavior.* ***Practical value.*** *The model serves as a practical tool for engineers designing control systems for renewable energy integration. By enhancing controller robustness, it contributes to more stable and reliable power systems in weak grid environments.* References 22, tables 2, figures 6.

Key words: **grid-connected inverter, weak grid, state-space model, small-signal analysis, phase locked loop, renewable energy.**

Вступ. *Стійкість мережевих інверторів є критично важливою для інтеграції відновлюваних джерел енергії в сучасні електроенергетичні системи. Однак ця стійкість суттєво погіршується в умовах слабкої електричної мережі, що характеризується високим імпедансом і низьким коефіцієнтом короткого замикання.* ***Проблема***. *За таких умов виникають складні динамічні взаємодії між системою керування інвертора, електричною мережею та фазовим автопідстроюванням частоти, що є ключовим для синхронізації. Ці взаємодії можуть погіршувати відстеження фази та навіть призводити до нестійкості системи. Такі складні ефекти роблять традиційні моделі недостатніми для точного оцінювання поведінки системи та розроблення робастних алгоритмів керування.* ***Мета*** *роботи полягає у розробленні та валідації компактної лінеаризованої моделі мережевого інвертора у просторі станів в умовах слабкої мережі, що дозволяє виконувати аналіз стійкості та підтримує синтез робастних стратегій керування.* ***Методика***. *На основі методу малих сигналів отримано представлення системи інвертора у просторі станів з урахуванням динаміки системи керування, імпедансу мережі та силового перетворювача. Точність моделі підтверджено шляхом детального нелінійного моделювання, що забезпечує високу узгодженість між двома підходами.* ***Результати***. *Запропонована модель ефективно відтворює взаємодію між динамікою інвертора та характеристиками слабкої мережі. Результати моделювання демонструють високу відповідність нелінійній поведінці, що підтверджує адекватність моделі.* ***Наукова новизна***. *На відміну від існуючих підходів, запропонована узагальнена лінеаризована модель у просторі станів явно враховує перехресні зв'язки між контурами керування та динамікою мережі в умовах слабкої мережі. Це забезпечує більш точний аналіз стійкості та глибше розуміння динамічних процесів у системі.* ***Практична значимість***. *Запропонована модель є ефективним інструментом для інженерів при розробленні систем керування для інтеграції відновлюваних джерел енергії. Підвищення робастності регуляторів сприяє забезпеченню більш стабільної та надійної роботи електроенергетичних систем в умовах слабких мереж.* Бібл. 22, табл. 2, рис. 6.

Ключові слова: **мережевий інвертор, слабка електромережа, модель простору станів, аналіз малих сигналів, фазове автопідстроювання частоти, відновлювана енергетика.**

Introduction. The increasing penetration of renewable energy sources has fundamentally transformed modern power system architecture and operation [1, 2]. A key element of this transformation is the widespread use of grid-connected inverters, which interface variable renewable generation, such as photovoltaic and wind energy systems, with the power grid [3–5]. These inverters are generally operated under current control and are responsible for delivering both active and reactive power, while ensuring synchronization with the grid voltage [6].

However, under weak grid conditions characterized by high grid impedance and low short-circuit capacity the dynamic interaction between inverter control systems and the grid becomes significantly more complex [7–10]. The phase-locked loop (PLL), which is critical for synchronizing the inverter with the grid, becomes highly sensitive to variations in grid impedance [11, 12]. This sensitivity may lead to degraded phase tracking, oscillatory responses, and even loss of synchronism, ultimately compromising system stability [9, 10]. Furthermore, the nonlinear behavior of power electronic interfaces and the tight coupling between inverter control loops and grid dynamics further intensify these challenges [11, 13].

Therefore, developing robust modeling and control approaches that ensure stable operation under weak grid conditions is a critical and timely challenge for integrating renewable energy sources into modern power systems.

To address the stability and control issues posed by weak grids, various strategies have been proposed. For example, in [4] was introduced an optimal virtual impedance control method to enhance system stability and improve reactive power sharing among distributed generation units. In [10], a variable virtual inductance control approach was presented to improve PLL damping and enhance dynamic performance. Another study [7] explored the interaction between PLL and current control during severe voltage sags and proposed a damping controller integrated within the active current loop.

Despite these advancements, accurate dynamic modeling of grid-connected inverters remains a foundational requirement for robust control design and system analysis. Two main approaches dominate the literature:

- small-signal modeling, which involves linearizing nonlinear system dynamics around an operating point [4, 5, 14, 15].
- impedance-based modeling, which characterizes the frequency-domain behavior of the inverter-grid interface [16–18].

Among these, small-signal models provide detailed insights into stability margins, resonance modes, and control sensitivities by simplifying nonlinear behavior into a tractable linear framework.

However, many existing models either oversimplify certain dynamic elements. This limits their effectiveness in analyzing and designing control strategies under highly dynamic or weak grid scenarios. Therefore, there is a clear need for a comprehensive, integrated small-signal state-space model that captures all significant dynamic interactions in such conditions.

The **goal** of this work is to develop and validate a compact, linearized state-space model of a grid-connected inverter under weak grid conditions, enabling stability analysis and supporting the design of robust control strategies.

This model aims to:

- accurately represent key dynamic behaviors during weak grid operation;
- provide a foundation for systematic stability analysis;
- support the design and tuning of robust control strategies.

To validate the proposed model, simulation studies are performed and compared against detailed nonlinear time-domain simulations, demonstrating close agreement and confirming the model's effectiveness.

Description of the studied system. Figure 1 shows the topology of a single voltage source converter (VSC) connected to an infinite bus through a transmission line. The converter voltage is assumed to be 3-phase symmetrical with no harmonic injection [19].

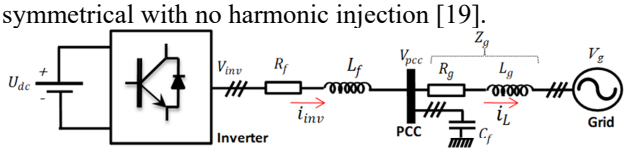

Fig. 1. Typical configuration of grid connected inverter

The inverter is connected to the bus through an LC filter with components R_f, L_f and C_f. R_g and L_g are the resistance and inductance of the transmission line respectively. V_{inv} and V_{pcc} are the voltage of the output inverter and point of common coupling (PCC); i_{inv} is the current across the converter; V_g is the voltage of the infinite source with the fixed system angular frequency marked as ω, fixed amplitude and the initial phase angle of zero.

The current components i_{inv}^{d} and i_{inv}^{q} are regulated using PI controllers. The reference currents i_{inv}^{dref} and i_{inv}^{qref} are typically generated by outer control loops, such as the active and reactive power control loops. However, in this paper, the analysis of the outer control loops is considered beyond the scope of the study. The simplified PLL model is shown in Fig 2,*b*. With PI controller, the quadrature voltage at PCC point equals zero and the voltage phase angle can be accurately locked and measured [20].

In Fig. 1 the stiffness of the grid at the PCC can be described by the short circuit ratio (SCR):

$$SCR = S_{SC}/S_N\,, \tag{1}$$

where S_{SC} is the short-circuit apparent power at the PCC; S_N is the total rated apparent power of inverters. Alternatively, the SCR can be expressed using voltage and current and line impedance Z_g as:

$$SCR = \frac{(3/2)V_g^2/|Z_g|}{(3/2)V_{pcc(rated)}\cdot i_{inv(rated)}} \approx \frac{V_g}{|Z_g|\cdot i_{inv(\max)}}, \tag{2}$$

where V_g is the amplitude of grid voltage; $V_{pcc(rated)}$ and $i_{inv(rated)}$ are the amplitude of the rated PCC voltage and rated inverter current.

From (2), it follows that the SCR decreases with increasing grid impedance Z_g. According to IEEE Standard 1204-1997, a system is regarded as a weak when $2<SCR<3$ [21].

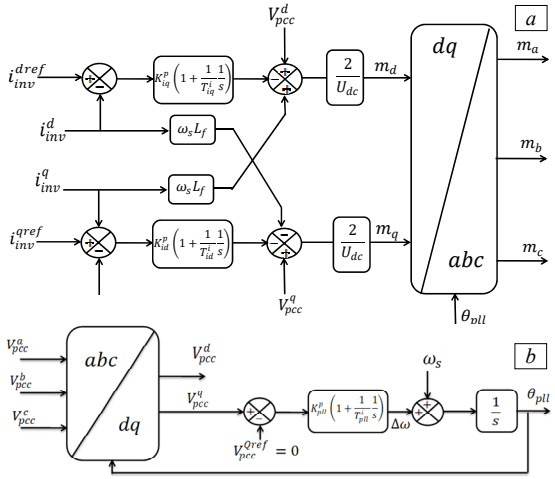

Fig. 2. Control diagram of grid connected inverter [19]: *a* – vector current control model; *b* – the simplified model of PLL

System modeling. To derive an accurately model of the grid-connected inverter in a weak grid environment, two distinct reference frames are employed [4]: the grid reference frame (*d*–*q*), which is synchronized with the actual grid voltage V_g, and the controller reference frame (*D*–*Q*) (Fig. 3), which is aligned with the estimated PCC voltage angle provided by the PLL [15].

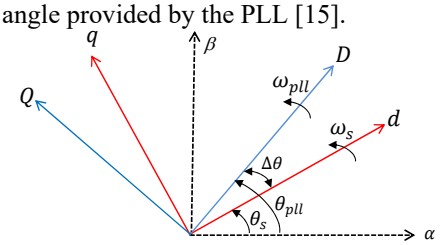

Fig. 3.Reference frame transformation

Under steady-state conditions, the controller's (*D*–*Q*) frame is aligned with the system's (*d*–*q*) frame. However, when small-signal perturbations affect the grid voltage, the orientation of the system (*d*–*q*) frame changes. Due to the PLL's internal dynamics particularly its PI regulator and the controller's (*D*–*Q*) frame may no longer remain aligned with the system (*d*–*q*) frame.

The following transformation matrix $T_{\Delta\theta}$ is used to convert system variables from the grid reference frame (*d*–*q*) to the controller reference frame (*D*–*Q*):

$$T_{\Delta\theta} = \begin{bmatrix} \cos(\Delta\theta) & \sin(\Delta\theta) \\ -\sin(\Delta\theta) & \cos(\Delta\theta) \end{bmatrix}, \tag{3}$$

where $\Delta\theta$ is the angular difference between the two frames. Here $\Delta\theta = \theta_{pll} - \theta_s$, $\theta_s = \omega_s t = 0$ represents the actual phase angle of the grid voltage, and θ_{pll} is the phase angle estimated by PLL.

For feedback control purposes, inverter voltage V_{inv}^{dq} and current i_{inv}^{dq} vectors expressed in the system *d*–*q* frame are transformed into the controller reference frame (*D*–*Q*) as follow:

$$\begin{bmatrix} V_{inv}^{D} \\ V_{inv}^{Q} \end{bmatrix} = \begin{bmatrix} \cos(\Delta\theta) & \sin(\Delta\theta) \\ -\sin(\Delta\theta) & \cos(\Delta\theta) \end{bmatrix} \begin{bmatrix} V_{inv}^{d} \\ V_{inv}^{q} \end{bmatrix}. \tag{4}$$

The duty-cycle commands (m_D, m_Q) generated by feedback control are then rotated to the system (*d*–*q*) frame by the applying the following inverse matrix:

$$T_{\Delta\theta}^{-1} = \begin{bmatrix} \cos(\Delta\theta) & -\sin(\Delta\theta) \\ \sin(\Delta\theta) & \cos(\Delta\theta) \end{bmatrix}. \tag{5}$$

1) *LC filter model*. The inverter system is modeled in the synchronous rotating reference frame (*d*–*q* aligned with the grid voltage orientation. The dynamics are derived for the inverter currents, PCC voltages, and grid-side currents, considering the LC filter and line impedances.

$$\begin{cases} \dfrac{\mathrm{d}i_{inv}^{d}}{\mathrm{d}t} = -\dfrac{R_f}{L_f} i_{inv}^{d} + \omega i_{inv}^{q} + \dfrac{V_{inv}^{d}}{L_f} - \dfrac{V_{pcc}^{d}}{L_f}; \\ \dfrac{\mathrm{d}i_{inv}^{q}}{\mathrm{d}t} = -\dfrac{R_f}{L_f} i_{inv}^{q} - \omega i_{inv}^{d} + \dfrac{V_{inv}^{q}}{L_f} - \dfrac{V_{pcc}^{q}}{L_f}; \\ \dfrac{\mathrm{d}V_{pcc}^{d}}{\mathrm{d}t} = \omega V_{pcc}^{q} + \dfrac{i_{inv}^{d}}{C_f} - \dfrac{i_{L}^{d}}{C_f}; \\ \dfrac{\mathrm{d}V_{pcc}^{q}}{\mathrm{d}t} = -\omega V_{pcc}^{d} + \dfrac{i_{inv}^{q}}{C_f} - \dfrac{i_{L}^{q}}{C_f}; \\ \dfrac{\mathrm{d}i_{L}^{d}}{\mathrm{d}t} = -\dfrac{R_g}{L_g} i_{L}^{d} + \omega i_{L}^{q} + \dfrac{V_{pcc}^{d}}{L_g} - \dfrac{V_{g}^{d}}{L_g}; \\ \dfrac{\mathrm{d}i_{L}^{q}}{\mathrm{d}t} = -\dfrac{R_g}{L_g} i_{L}^{q} - \omega i_{L}^{d} + \dfrac{V_{pcc}^{q}}{L_g} - \dfrac{V_{g}^{q}}{L_g}, \end{cases} \tag{6}$$

where R_f, C_f, L_f are the resistance, inductance, and capacitance of the inverter filter respectively; R_g, L_g are the resistance and inductance of the line impedance respectively; ω is the grid angular frequency; $i_{inv}^{d,q}$ is the inverter output current; $i_{L}^{d,q}$ is the load current in the (*d*–*q*) axis; $V_{pcc}^{d,q}$ is the voltage at the PCC; $V_{inv}^{d,q}$ is the inverter voltage in (*d*–*q*) reference frame.

The inverter output voltage is determined by the modulation indices m_d, m_q and the DC-link voltage U_{dc}:

$$\begin{cases} V_{inv}^{d} = m_d \dfrac{U_{dc}}{2}; \\ V_{inv}^{q} = m_q \dfrac{U_{dc}}{2}. \end{cases} \tag{7}$$

2) *Current controller loop modeling*. The current control loop employs a conventional PI controller. The controller receives as input the error signal, which is the difference between the measured (sampled) inverter output current and its reference value. In addition, a feed-forward term is introduced to compensate for disturbances in the output voltage. This control structure computes the modulation indices in the (*D*–*Q*) reference frame, denoted as (m_D, m_Q) which are then supplied to the PWM block. The control dynamics are described as:

$$\begin{cases} \dfrac{\mathrm{d}\eta_D}{\mathrm{d}t} = -\dfrac{1}{T_i^{i}} \left(i_{inv}^{Dref} - i_{inv}^{D} \right); \\ \dfrac{\mathrm{d}\eta_Q}{\mathrm{d}t} = -\dfrac{R_f}{L_f} \left(i_{inv}^{Qref} - i_{inv}^{Q} \right); \\ \dfrac{\mathrm{d}m_D}{\mathrm{d}t} = \dfrac{1}{T_s} \left(m'_D - m_D \right); \\ \dfrac{\mathrm{d}m_Q}{\mathrm{d}t} = \dfrac{1}{T_s} \left(m'_Q - m_Q \right); \\ m'_D = \dfrac{2}{U_{dc}} \left(\left(i_{inv}^{Dref} - i_{inv}^{D} + \eta_D \right) k_p^{i} + V_{pcc}^{D} - \omega L_f i_{inv}^{Q} \right); \\ m'_Q = \dfrac{2}{U_{dc}} \left(\left(i_{inv}^{Qref} - i_{inv}^{Q} + \eta_Q \right) k_p^{i} + V_{pcc}^{Q} + \omega L_f i_{inv}^{D} \right); \end{cases} \tag{8}$$

where i_{inv}^{Dref}, i_{inv}^{Qref} are the reference currents in the (*D*–*Q*) axis; i_{inv}^{D}, i_{inv}^{Q} are the actual inverter output currents in the *D*-axis and *Q*-axis (the controller's frame); η_D, η_Q are the integrator states (integral action of the current PI controller); m_D, m_Q are the actual modulation indices; m'_D, m'_Q are the calculated modulation indices; T_i^{i} is the integral time constant of the current PI controller; k_p^{i} is the proportional gain of the current PI controller; T_s is the modulation and calculation delay; $V_{pcc}^{D,Q}$ is the voltage at the PCC in (*D*–*Q*) reference frame.

3) *PLL dynamic modeling*. The PLL technique is essential for extracting phase and frequency information from the electrical system, particularly when interfacing with power electronic devices. The PLL block measures the system frequency and provides the phase synchronization angle to the reference frame transformation block, enabling control operations to be executed in synchronism with the power grid [22].

As illustrated in Fig. 2,*b* the controller operates in a rotating (*D*–*Q*) reference frame, which rotates at an angular frequency ω_{pll}, with the *d*-axis phase-aligned according to the angle θ_{pll}. This phase alignment is determined by the PLL.

The dynamics of the PLL can be described as:

$$\begin{cases} \dfrac{\mathrm{d}\varepsilon_Q}{\mathrm{d}t} = \dfrac{1}{T_{pll}^{i}} V_{pcc}^{Q}; \\ \dfrac{\mathrm{d}\theta_{pll}}{\mathrm{d}t} = k_{pll}^{p} \left(V_{pcc}^{Q} + \varepsilon_Q \right), \end{cases} \tag{9}$$

where θ_{pll} is the estimated phase angle of the grid voltage; T_{pll}^{i} is the integral time constant of the PLL controller; V_{pcc}^{Q} is the voltage at the PCC in *D*-axis; k_{pll}^{p} is the proportional gain of the PLL controller; ε_Q is the integral action state (internal variable for the PLL integrator).

4) *Full dynamic model*. The full dynamic model of the grid-connected inverter, incorporating the control system and the PLL, is formulated by combining the state equations (1) – (3), along with the transformation matrices $T_{\Delta\theta}$ and $T_{\Delta\theta}^{-1}$. This results in a comprehensive state-space representation that captures the electrical dynamics of the LC filter, the inverter control loops, and the synchronization mechanism. The system is expressed as a nonlinear differential equation of the form:

$$\mathrm{d}x / \mathrm{d}t = f(x, u), \tag{10}$$

where the state vector x is given by:

$$x = \left[i_{inv}^{d} \;\; i_{L}^{d} \;\; V_{pcc}^{d} \;\; i_{inv}^{q} \;\; i_{L}^{q} \;\; V_{pcc}^{q} \;\; \eta_D \;\; \eta_Q \;\; m_D \;\; m_Q \;\; \theta_{pll} \;\; \varepsilon_Q \right]^{T},$$

and the control input vector $u = \left[V_g^{d} \;\; V_g^{q} \;\; i_{inv}^{Dref} \;\; i_{inv}^{Qref} \right]^{T}$; $f(x, u)$ is the nonlinear function characterizing the system dynamics defined by (11).

The inherent complexity of the original nonlinear model, referred to as equations (10), (11), stems directly from the inclusion of the PLL dynamics, which introduce significant nonlinearities into the system's mathematical representation. These nonlinearities arise primarily from trigonometric functions involving the PLL angle and its coupling with other key state variables, such as currents and voltages. Consequently, the model becomes analytically intractable and poses substantial challenges for control design, stability analysis, and performance prediction.

$$f(x,u)=\begin{bmatrix}
-\frac{1}{L_f}\left(V_{pcc}^{d}+R_f i_{inv}^{d}-\omega L_f i_{inv}^{q}-m_D\frac{U_{dc}}{2}\cos\left(\theta_{pll}\right)+m_Q\frac{U_{dc}}{2}\sin\left(\theta_{pll}\right)\right)\\
\frac{1}{L_g}\left(V_{pcc}^{d}-V_g^{d}-R_g i_L^{d}+\omega L_g i_L^{q}\right)\\
\frac{1}{C_f}\left(i_{inv}^{d}-i_L^{d}+\omega C_f V_{pcc}^{q}\right)\\
-\frac{1}{L_f}\left(V_{pcc}^{q}+R_f i_{inv}^{q}+\omega L_f i_{inv}^{d}-m_Q\frac{U_{dc}}{2}\cos\left(\theta_{pll}\right)-m_D\frac{U_{dc}}{2}\sin\left(\theta_{pll}\right)\right)\\
\frac{1}{L_g}\left(V_{pcc}^{q}-V_g^{q}-R_g i_L^{q}-\omega L_g i_{pL}^{d}\right)\\
\frac{1}{C_f}\left(i_{inv}^{q}-i_L^{q}-\omega C_f V_{pcc}^{d}\right)\\
\frac{1}{T_i^{i}}\left(i_{inv}^{Dref}-i_{inv}^{d}\cos\left(\theta_{pll}\right)-i_{inv}^{q}\cos\left(\theta_{pll}\right)\right)\\
\frac{1}{T_i^{i}}\left(i_{inv}^{Qref}-i_{inv}^{q}\cos\left(\theta_{pll}\right)+i_{inv}^{d}\sin\left(\theta_{pll}\right)\right)\\
\frac{1}{T_s}\left(\frac{2}{U_{dc}}\left(\left(i_{inv}^{Dref}-i_{inv}^{d}\cos\left(\theta_{pll}\right)-i_{inv}^{q}\sin\left(\theta_{pll}\right)+\eta_D\right)k_p^{i}+V_{pcc}^{d}\cos\left(\theta_{pll}\right)+V_{pvv}^{q}\sin\left(\theta_{pll}\right)-\omega L_f i_{inv}^{q}\cos\left(\theta_{pll}\right)+\omega L_f i_{inv}^{d}\sin\left(\theta_{pll}\right)\right)-m_D\right)\\
\frac{1}{T_s}\left(\frac{2}{U_{dc}}\left(\left(i_{inv}^{Qref}-i_{inv}^{q}\cos\left(\theta_{pll}\right)+i_{inv}^{q}\cos\left(\theta_{pll}\right)+\eta_Q\right)k_p^{i}+V_{pcc}^{q}\cos\left(\theta_{pll}\right)-V_{pll}^{d}\sin\left(\theta_{pll}\right)+\omega L_f i_{inv}^{d}\cos\left(\theta_{pll}\right)+\omega L_f i_{inv}^{q}\sin\left(\theta_{pll}\right)\right)-m_Q\right)\\
k_{pll}^{p}\left(\varepsilon_Q-V_{pcc}^{d}\sin\left(\theta_{pll}\right)+V_{pcc}^{q}\cos\left(\theta_{pll}\right)\right)\\
\frac{1}{T_{pll}^{i}}\left(V_{pll}^{q}\cos\left(\theta_{pll}\right)-V_{pll}^{d}\sin\left(\theta_{pll}\right)\right)
\end{bmatrix}. \quad (11)$$

To address these challenges and establish a framework amenable to rigorous analysis and systematic controller synthesis, we justify the development of a simplified linearized model using the well-established Jacobian linearization technique. This approach is widely accepted and formally valid under the assumption that the system operates near a stable equilibrium point, denoted as (x_0, u_0), where the nonlinear functions are smooth and continuously differentiable.

The outcome of this process is a linear time-invariant model, presented as equation (12), which offers several critical advantages over its nonlinear counterpart. Most notably, it enables the application of powerful linear systems theory, facilitating:

- advanced stability analysis (e.g., eigenvalue-based assessment);
- facilitate the design and systematic tuning of robust control strategies, thereby enhancing stability margins in weak grid scenarios

Linearized state-space model is carried out around a steady-state operating point. This process results in a linear time-invariant model that accurately captures the system dynamics in the vicinity of the equilibrium. The state-space representation of the linearized system is obtained by linearizing equation (11) around the operating point (x_0, u_0), as given by:

$$\frac{\mathrm{d}\Delta x}{\mathrm{d}t}=A\cdot\Delta x+B\cdot\Delta u\ , \quad (12)$$

where $\Delta x=x-x_0$ is the deviation from the steady-state state vector; $\Delta u=u-u_0$ is the input perturbation; A, B are the Jacobian matrices of the system dynamics, they are computed as:

$$A=\frac{\partial}{\partial x}f(x,u)\bigg|_{x_0,u_0}\ ;\ B=\frac{\partial}{\partial u}f(x,u)\bigg|_{x_0,u_0}\ . \quad (13)$$

The full analytical expressions for the matrices A and B are provided in Appendix in equations (A.1) and (A.2), respectively.

Simulation results. A simulation study was conducted using MATLAB/Simulink to validate the theoretical analysis discussed earlier. Both the power stage and control system were modeled within the simulation environment. Key simulation parameters, including the operating point of the VSC system and the associated power controller settings, are listed in Table 1.

Table 1

Parameters of VSC connected to weak grid

	Parameters symbols	Value
Main circuit parameters	Equivalent AC source voltage V_g (line-to-line RMS)	380 V
	Inverter rated current	60 A
	Nominal utility frequency f_s	50 Hz
	Equivalent line transmission impedance R_g+jx_g	0.302+j1.6022 Ω
	LC filter capacitor C_f	240 μF
	LC filter inductance L_f	0.02+j0.1751 Ω
	Rated DC voltage U_{dc}	700 V
Controllers parameters	Current controller gains (T_i^i, k_i^p)	0.1426, 20
	PLL controller gains (T_{pll}^i, k_{pll}^p)	0.1070, 27

To verify the linearized state-space model, the time-domain response of a VSC connected to an AC grid was computed using the small-signal model in MATLAB. This response was then compared to that obtained from the full nonlinear model implemented in Simulink.

The state-space matrices A and B in (12) were

computed using the expressions provided in Appendix, based on the system parameters and the specific operating point under consideration.

Test scenarios. To validate the accuracy of the developed state-space model, small perturbations were introduced around three distinct operating points. The resulting dynamic responses from the state-space model were then compared to those obtained from a full nonlinear simulation. This comparison was conducted to assess the fidelity of the linearized model in capturing the system's transient and steady-state behavior.

Table 2 illustrates the profiles of the *d*-axis and *q*-axis reference currents i_{inv}^{dref} and i_{inv}^{qref} used as input perturbations during the validation process.

Table 2

Inverter reference currents profiles for three test scenarios

Time, s	1st test		2nd test		3rd test	
	i_{inv}^{dref}, A	i_{inv}^{qref}, A	i_{inv}^{dref}, A	i_{inv}^{qref}, A	i_{inv}^{dref}, A	i_{inv}^{qref}, A
0	–50	0	–50	–10	–50	+10
0.8	–55		–55		–55	
0.9	–50		–50		–50	
1	–45		–45		–45	

The *d*-axis reference current i_{inv}^{dref} signal exhibits step changes at approximately 0.8 s, 0.9 s and 1 s. The perturbation amplitude varies within ±5 A around the operating point of i_{inv}^{dref} = –50 A for three test scenarios. These variations represent active power reference changes, as i_{inv}^{dref} typically corresponds to active power flow in a grid-connected VSC system. The negative sign of the current reference indicates that active power is injected from the inverter to the grid. The *q*-axis reference current component i_{inv}^{qref} remains constant for each of the three operating points, taking values of 0 A, –10 A and +10 A, respectively. These values represent, in order, no reactive power exchange, reactive power absorption, and reactive power injection.

Figures 4–6 present the dynamic responses of the load current. The response of the linearized state-space model is compared with that obtained from the full nonlinear simulation for three different test scenarios (see Table 2), in order to evaluate the accuracy of the developed model. The system is assumed to initially operate around an equilibrium point characterized by the load current components i^{d}_{L0} and i^{q}_{L0} in the *d*–*q* reference frame. This operating point is then disturbed by applying a small variation of Δi_{inv}^{dref} = ±5 A to the *d*-axis reference current (–50 A). The resulting load current responses in both the *d*-axis and *q*-axis are then observed.

The comparison shows a strong agreement between the two models. The minor deviations observed in the *q*-axis load current under steady-state conditions remain negligible, confirming the ability of the linearized model to faithfully reproduce the system dynamics and thereby validating its accuracy around the selected operating points.

Figure 4 shows the dynamic responses of the linearized state-space model and the detailed simulation model for the 1st test scenario. In this case, a disturbance is applied to i_{inv}^{dref}, while i_{inv}^{qref} is kept at 0 A. Figure 4 shows an almost identical response between the two models, particularly in transient oscillations and steady-state convergence. This confirms the linear model's ability to capture the system behavior around this operating point.

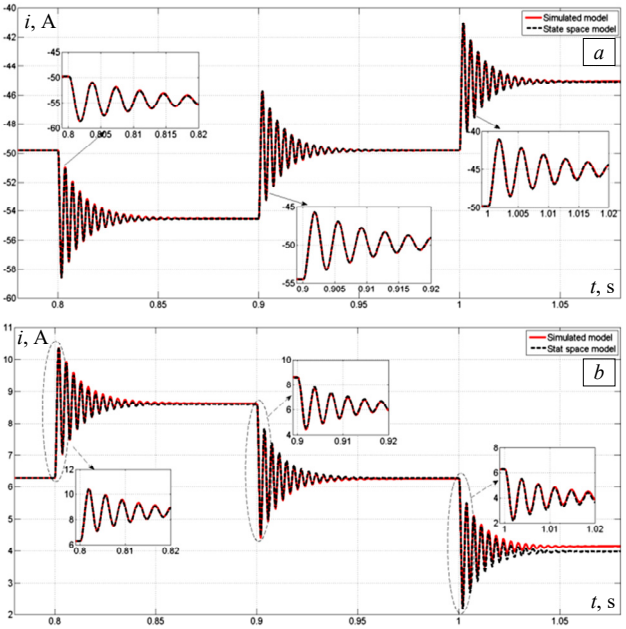

Fig. 4. Dynamic responses of the state-space model and detailed simulation model for the 1st test: *a* – load current response in the *d*-axis; *b* – load current response in the *q*-axis

Figure 5 shows the dynamic responses of the linearized state-space model and the detailed simulation model for the 2nd test scenario. Here, the same *d*-axis perturbation is applied, but the *q*-axis current reference is set to a negative value, i_{inv}^{qref} = –10 A. The results show that the linearized model closely tracks the full simulation, even during rapid transients and dynamic interactions between the *d* and *q* axes.

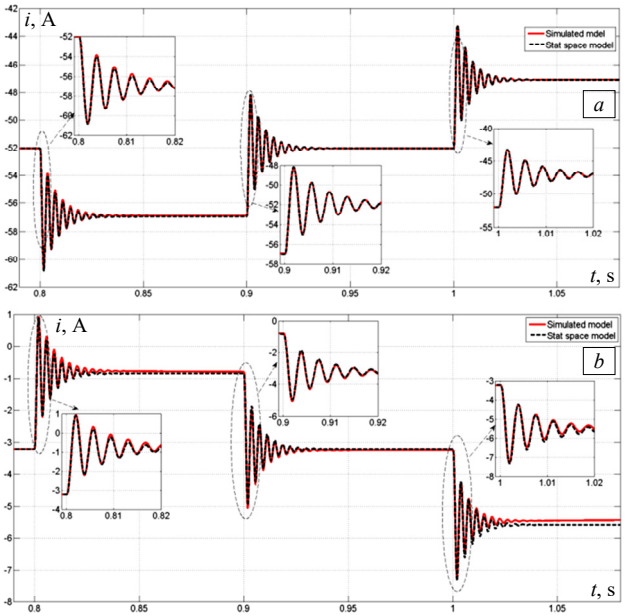

Fig. 5. Dynamic responses of the state-space model and detailed simulation model for the 2end test: *a* – Load current response in the *d*-axis; *b* – load current response in the *q*-axis

Figure 6 shows the dynamic responses of the linearized state-space model and the detailed simulation

model for the 3rd test scenario. In this case, the same perturbation on is applied, but the q-axis current reference is set to a positive value, i_{inv}^{qref} = +10 A, introducing a different dynamic condition. Again, the linearized model demonstrates excellent agreement with the full simulation, confirming its ability to accurately replicate system dynamics under varying operating conditions.

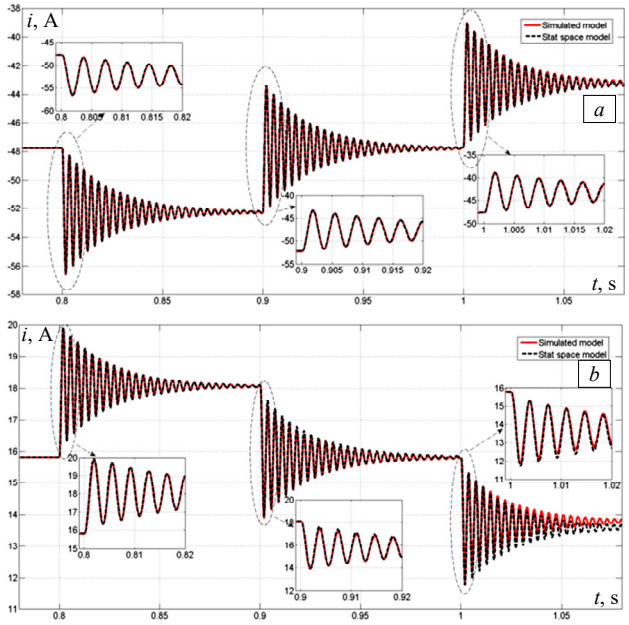

Fig. 6. Dynamic responses of the state-space model and detailed simulation model for the 3rd test: *a* – load current response in the *d*-axis; *b* – load current response in the *q*-axis

Figures 4–6 also emphasize the significant influence of the q-axis reference current on the damping behavior of load current oscillations. Specifically, when i_{inv}^{qref} is positive corresponding to reactive power absorption by the inverter, the system exhibits weaker damping compared to cases where i_{inv}^{qref} is negative, resulting in a reduced stability margin. However, a detailed analysis of the impact of these parameters on system dynamics lies beyond the scope of this study. The primary objective of this work is to develop a model capable of accurately reproducing both the dynamic and steady-state behavior of grid-connected inverters under weak grid conditions. Future research could focus on a more in-depth investigation of how operating conditions, control parameters, and line characteristics influence the system's stability and dynamic response.

Conclusions. This work has successfully achieved its goal of developing and validating a compact, linearized state-space model for grid-connected inverter operating in weak grid conditions. The proposed model incorporates the essential dynamics of inverter control systems, including the PLL, current control loops, converter filter and grid impedance. Using small-signal analysis, the model was derived and its accuracy confirmed through detailed nonlinear simulations in MATLAB/Simulink under multiple operating scenarios.

The simulation results demonstrate strong agreement between the linearized and nonlinear models in both transient and steady-state responses, validating the model's capability to capture key dynamic behavior near the operating point. Furthermore, analysis of the q-axis reference current revealed its significant impact on system damping. Specifically, a positive q-axis current associated with reactive power absorption was shown to reduce damping and stability margins, emphasizing the need for careful control tuning under weak grid conditions.

The model can serve as a practical tool for control design and stability assessment in weak grid scenarios. Also, control parameters such as PLL bandwidth and current loop gains should be tuned based on dynamic stability analysis to prevent oscillatory behavior or loss of synchronism.

Future work will explore the influence of control parameter variations, line impedance characteristics, and grid strength fluctuations on system stability. Further research will focus on using the model to design and optimize adaptive or robust control schemes for grid-connected inverters operating under a wide range of grid conditions.

These developments will enhance the reliability and resilience of renewable energy systems in weak and evolving power networks.

Appendix. The full expressions of matrices A and B are given below:

$$A=\begin{bmatrix}
-\frac{R_f}{L_f} & 0 & -\frac{1}{L_f} & \omega_0 & 0 & 0 & 0 & 0 & \frac{U_{dc}}{2L_f}a & -\frac{U_{dc}}{2L_f}b & -\frac{1}{L_f}\left(m_{D0}\frac{U_{dc}}{2}b+m_{Q0}\frac{U_{dc}}{2}a\right) & 0\\
0 & -\frac{R_g}{L_g} & \frac{1}{L_g} & 0 & \omega_0 & 0 & 0 & 0 & 0 & 0 & 0 & 0\\
\frac{1}{C_f} & -\frac{1}{C_f} & 0 & 0 & 0 & \omega_0 & 0 & 0 & 0 & 0 & 0 & 0\\
-\omega_0 & 0 & 0 & -\frac{R_f}{L_f} & 0 & -\frac{1}{L_f} & 0 & 0 & \frac{U_{dc}}{2L_f}b & \frac{U_{dc}}{2L_f}a & \frac{U_{dc}}{2L_f}\left(-m_{Q0}b+m_{D0}a\right) & 0\\
0 & -\omega_0 & 0 & 0 & -\frac{R_g}{L_g} & \frac{1}{L_g} & 0 & 0 & 0 & 0 & 0 & 0\\
0 & 0 & -\omega_0 & \frac{1}{C_f} & -\frac{1}{C_f} & 0 & 0 & 0 & 0 & 0 & 0 & 0\\
-\frac{a}{T_i^i} & 0 & 0 & -\frac{b}{T_i^i} & 0 & 0 & 0 & 0 & 0 & 0 & \frac{1}{T_i^i}\left(i_{inv0}^d b-i_{inv0}^q a\right) & 0\\
\frac{b}{T_i^i} & 0 & 0 & -\frac{a}{T_i^i} & 0 & 0 & 0 & 0 & 0 & 0 & \frac{1}{T_i^i}\left(i_{inv0}^q b+i_{inv0}^d a\right) & 0\\
-\frac{2}{T_sU_{dc}}\left(k_p^i a-\omega_0 L_f b\right) & 0 & \frac{2}{T_sU_{dc}}a & -\frac{2}{T_sU_{dc}}\left(k_p^i b+\omega_0 L_f a\right) & 0 & \frac{2}{T_sU_{dc}}b & \frac{2}{T_sU_{dc}}k_p^i & 0 & -\frac{1}{T_s} & 0 & \frac{2}{T_sU_{dc}}\left(-i_{inv0}^d k_p^i a-i_{inv0}^q k_p^i b+V_{pcc0}^d a+V_{pcc0}^q b-\omega_0 L_f i_{inv0}^q a+\omega_0 L_f i_{inv0}^d b\right) & 0\\
\frac{2}{T_sU_{dc}}\left(k_p^i b+\omega_0 L_f a\right) & 0 & -\frac{2}{T_sU_{dc}}b & -\frac{2}{T_sU_{dc}}\left(k_p^i a-\omega_0 L_f b\right) & 0 & \frac{2}{T_sU_{dc}}a & 0 & \frac{2}{T_sU_{dc}} & 0 & -\frac{1}{T_s} & \frac{2}{T_sU_{dc}}\left(-i_{inv0}^d k_p^i a-i_{inv0}^q k_p^i b+V_{pcc0}^d a+V_{pcc0}^q b-\omega_0 L_f i_{inv0}^q a+\omega_0 L_f i_{inv0}^d b\right) & 0\\
0 & 0 & -k_{pll}^p b & 0 & 0 & k_{pll}^p a & 0 & 0 & 0 & 0 & -k_{pll}^p\left(V_{pcc0}^d a+V_{pcc0}^q b\right) & k_{pll}^p\\
0 & 0 & -\frac{1}{T_{pll}^i}b & 0 & 0 & \frac{1}{T_{pll}^i}a & 0 & 0 & 0 & 0 & -\frac{1}{T_{pll}^i}\left(V_{pcc0}^q b+V_{pcc0}^d a\right) & 0
\end{bmatrix} \quad \text{(A.1)}$$

$$B = \begin{bmatrix} 0 & 0 & 0 & 0 \\ -1/L_g & 0 & 0 & 0 \\ 0 & 0 & 0 & 0 \\ 0 & 0 & 0 & 0 \\ 0 & -1/L_g & 0 & 0 \\ 0 & 0 & 0 & 0 \\ 0 & 0 & 1/T_i^i & 0 \\ 0 & 0 & 0 & 1/T_i^i \\ 0 & 0 & 2/T_s U_{dc} & 0 \\ 0 & 0 & 0 & 2/T_s U_{dc} \\ 0 & 0 & 0 & 0 \\ 0 & 0 & 0 & 0 \end{bmatrix}, \quad (A.2)$$

where a and b in the matrix A are:

$$a = \sin(\theta_{pll0}); \quad (A.3)$$

$$b = \cos(\theta_{pll0}). \quad (A.4)$$

The subscript «0» indicates the equilibrium point around which the system has been linearized. This steady-state point, denoted as x_0, is obtained by numerically solving the nonlinear equation (10) using the *solve* function in MATLAB.

Conflict of interest. The authors declare that they have no conflicts of interest.

REFERENCES

1. Janardhan G., Surendra Babu N.N.V., Srinivas G.N. Single phase transformerless inverter for grid connected photovoltaic system with reduced leakage current. *Electrical Engineering & Electromechanics*, 2022, no. 5, pp. 36-40. doi: https://doi.org/10.20998/2074-272X.2022.5.06.

2. Boukadoum A., Bouguerne A., Bahi T. Direct power control using space vector modulation strategy control for wind energy conversion system using three-phase matrix converter. *Electrical Engineering & Electromechanics*, 2023, no. 3, pp. 40-46. doi: https://doi.org/10.20998/2074-272X.2023.3.06.

3. Xie J. Application of optimized photovoltaic grid-connected control system based on modular multilevel converters. *Energy Informatics*, 2024, vol. 7, no. 1, art. no. 24. doi: https://doi.org/10.1186/s42162-024-00317-3.

4. Bennia I., Daili Y., Harrag A., Alrajhi H., Saim A., Guerrero J.M. Stability and Reactive Power Sharing Enhancement in Islanded Microgrid via Small-Signal Modeling and Optimal Virtual Impedance Control. *International Transactions on Electrical Energy Systems*, 2024, vol. 2024, art. no. 5469868. doi: https://doi.org/10.1155/2024/5469868.

5. Ji X., Liu D., Jiang K., Zhang Z., Yang Y. Small-Signal Stability of Hybrid Inverters with Grid-Following and Grid-Forming Controls. *Energies*, 2024, vol. 17, no. 7, art. no. 1644. doi: https://doi.org/10.3390/en17071644.

6. Muthukaruppasamy S., Dharmaprakash R., Sendilkumar S., Parimalasundar E. Enhancing off-grid wind energy systems with controlled inverter integration for improved power quality. *Electrical Engineering & Electromechanics*, 2024, no. 5, pp. 41-47. doi: https://doi.org/10.20998/2074-272X.2024.5.06.

7. Wang X., Yao J., Pei J., Sun P., Zhang H., Liu R. Analysis and Damping Control of Small-Signal Oscillations for VSC Connected to Weak AC Grid During LVRT. *IEEE Transactions on Energy Conversion*, 2019, vol. 34, no. 3, pp. 1667-1676. doi: https://doi.org/10.1109/TEC.2019.2915680.

8. Zheng Y., Han Y., Wang C., Ren Q., Yang P., Zalhaf A.S. Impact of phase-locked loop on grid-connected inverter stability under weak grid conditions and suppression measures. *Computers and Electrical Engineering*, 2025, vol. 123, art. no. 110249. doi: https://doi.org/10.1016/j.compeleceng.2025.110249.

9. Tamari Y., Kato T., Inoue K. Stability Analysis Considering PLL Effects for Grid-Following Inverter by Complex Vector Control. *IEEJ Transactions on Electronics, Information and Systems*, 2024, vol. 144, no. 11, pp. 1044-1051. doi: https://doi.org/10.1541/ieejeiss.144.1044.

10. Liu A., Cao H., Liu J. Enhancing stability control of Phase-Locked loop in weak power grids. *International Journal of Electrical Power & Energy Systems*, 2024, vol. 161, art. no. 110145. doi: https://doi.org/10.1016/j.ijepes.2024.110145.

11. Zhang Y., Pen H., Zhang X. Stability Control of Grid-Connected Converter Considering Phase-Locked Loop Frequency Coupling Effect. *Energies*, 2024, vol. 17, no. 14, art. no. 3438. doi: https://doi.org/10.3390/en17143438.

12. Yue J., Gao J., An R., Jin L., Tao R., Zou K. A Method for Improving the Stability of Grid-Connected Inverters by Eliminating the Negative Effects of PLL in Weak Grids. *2022 4th International Conference on Power and Energy Technology (ICPET)*, 2022, pp. 299-304. doi: https://doi.org/10.1109/ICPET55165.2022.9918343.

13. Lin X., Chih-Hsien Peng J., Macii D., Petri D., Yu J., Wen H. Frequency-domain small-signal stability analysis methods for grid-following converters systems – An overview. *Renewable and Sustainable Energy Reviews*, 2025, vol. 211, art. no. 115283. doi: https://doi.org/10.1016/j.rser.2024.115283.

14. Pathan E., Zulkifli S.A., Tayab U.B., Jackson R. Small Signal Modeling of Inverter-based Grid-Connected Microgrid to Determine the Zero-Pole Drift Control with Dynamic Power Sharing Controller. *Engineering, Technology & Applied Science Research*, 2019, vol. 9, no. 1, pp. 3790-3795. doi: https://doi.org/10.48084/etasr.2465.

15. Zou Z.-X., Rosso R., Liserre M. Modeling of the Phase Detector of a Synchronous-Reference-Frame Phase-Locked Loop Based on Second-Order Approximation. *IEEE Journal of Emerging and Selected Topics in Power Electronics*, 2020, vol. 8, no. 3, pp. 2534-2545. doi: https://doi.org/10.1109/JESTPE.2019.2920309.

16. Pérez-Estévez D., Ríos-Castro D., Fernández-Abraldes P.M., Monteiro V., Pinto J.G., Afonso J.L., Doval-Gandoy J. Asymmetric Impedance Model for Grid-Forming Converters With Droop Control. *IEEE Transactions on Power Electronics*, 2025, vol. 40, no. 9, pp. 12977-12997. doi: https://doi.org/10.1109/TPEL.2025.3565789.

17. Golestan S., Ebrahimzadeh E., Wen B., Guerrero J.M., Vasquez J.C. dq-Frame Impedance Modeling of Three-Phase Grid-Tied Voltage Source Converters Equipped With Advanced PLLs. *IEEE Transactions on Power Electronics*, 2021, vol. 36, no. 3, pp. 3524-3539. doi: https://doi.org/10.1109/TPEL.2020.3017387.

18. Lu S., Zhu Y., Dong L., Na G., Hao Y., Zhang G., Zhang W., Cheng S., Yang J., Sui Y. Small-Signal Stability Research of Grid-Connected Virtual Synchronous Generators. *Energies*, 2022, vol. 15, no. 19, art. no. 7158. doi: https://doi.org/10.3390/en15197158.

19. Fang L., Feng L., Chu C., Xu J., Wu R., Fan Q. Evaluation of dominant factors for stability of grid-connected inverters based on impedance sensitivity analysis. *IET Renewable Power Generation*, 2024, vol. 18, no. 16, pp. 3788-3797. doi: https://doi.org/10.1049/rpg2.13020.

20. Gassara K., Gassara B., Fakhfakh A., De Pablo S. Offline Analysis of a Modified dqPLL Architecture based on THD Compensation Blocks for Three-Phase Grid-Tied Inverters. *Engineering, Technology & Applied Science Research*, 2025, vol. 15, no. 3, pp. 22669-22677. doi: https://doi.org/10.48084/etasr.10206.

21. Pal D., Panigrahi B.K. A Nonlinear Adaptive Stabilizing Control Strategy to Enhance Dynamic Stability of Weak Grid-Tied VSC System. *IEEE Transactions on Power Delivery*, 2022, vol. 37, no. 3, pp. 2182-2193. doi: https://doi.org/10.1109/TPWRD.2021.3106682.

22. Zerzouri N., Ben Si Ali N., Benalia N. A maximum power point tracking of a photovoltaic system connected to a three-phase grid using a variable step size perturb and observe algorithm. *Electrical Engineering & Electromechanics*, 2023, no. 5, pp. 37-46. doi: https://doi.org/10.20998/2074-272X.2023.5.06.

Received 01.09.2025
Accepted 08.12.2025
Published 02.05.2026

Y. Daili [1], *Associate Professor,*
R. Bentafer[1,3], *PhD,*
N. Djaraf [1,3], *PhD,*
A. Harrag [2,3], *Professor,*
[1] Electrotechnics Department, Faculty of Technology,
Ferhat Abbas University Setif 1, 19000 Setif, Algeria,
e-mail: yassine.daili@univ-setif.dz (Corresponding Author)
[2] Electronics Department, Faculty of Technology,
Ferhat Abbas University Setif 1, 19000 Setif, Algeria.
[3] Mechatronics Laboratory (LMETR), Optics and Precision Mechanics Institute, Ferhat Abbas University Setif 1, Setif, Algeria.

How to cite this article:
Daili Y., Bentafer R., Djaraf N., Harrag A. Comprehensive modeling of grid-connected inverters in weak grid systems. *Electrical Engineering & Electromechanics*, 2026, no. 3, pp. 42-48. doi: https://doi.org/10.20998/2074-272X.2026.3.06